JASA ARTICLE

# Laser ultrasonic investigation of chromium coating impact on elastic guided waves in zirconium tubes

Hafsa Diboune,[1,2,a)] Daniel A. Kiefer,[1] Florian Lyonnet,[2] Pierre Barberis,[3] François Bruno,[1] Sylvain Mezil,[1] and Claire Prada[1]

[1]*Institut Langevin, ESPCI Paris, Université PSL, CNRS, 75005 Paris, France*

[2]*Site de Paimboeuf, Framatome, 44560 Paimboeuf, France*

[3]*Centre de Recherche Composants, Framatome, Avenue Paul Girod, 73400 Ugine, France*

**ABSTRACT:**

The impact of a chromium (Cr) coating on the elastic guided waves propagating in zirconium alloy (called M5 Framatome and referred to as M5 hereafter) nuclear cladding tubes is studied both theoretically and experimentally. Longitudinal modes are measured on different 9.5 mm–diameter tubes by a non-contact laser ultrasonic technique. These modes are calculated using the M5 elastic constants determined from x-ray diffraction measurements. Since Cr has a much higher shear wave velocity than the M5 alloy, the dispersion of observed guided modes is significantly modified by the coating. In the mid-frequency range, characterized by shear wavelengths on the order of the tube thickness, the second longitudinal mode appears to be particularly sensitive to the coating. In a higher frequency range, it is observed that modes are well measured in a frequency-wavenumber domain corresponding to the leaky surface wave of a Cr coated infinite M5 substrate. A simple but effective model predicts the observability of each mode, in good qualitative agreement with experimental observations. © *2026 Acoustical Society of America*.

https://doi.org/10.1121/10.0042186

(Received 26 June 2025; revised 12 December 2025; accepted 12 December 2025; published online 14 January 2026)

[Editor: Didier Dragna] Pages: 398–407

## I. INTRODUCTION

Safety is essential to the operation of nuclear facilities. It is of utmost importance to avoid all possible causes of damage to power plant components and particularly to fuel cladding tubes. The metal cladding surrounding the fuel must resist to the high mechanical, thermal, and neutronic stresses it encounters in the reactor core. Nuclear fuel developers have opted for zirconium alloys for cladding enriched uranium oxide pellets, as this material offers good mechanical and thermal strength, as well as a very small cross sectional area for absorbing thermal neutrons in pressurized water or boiling water reactors. To improve the mechanical properties of cladding tubes, a zirconium alloy called M5 Framatome (referred to as M5 hereafter) was introduced by Framatome in the 1990s. This alloy, containing niobium and various other additives, such as oxygen and iron, was also created to increase the resistance to high-temperature water corrosion and reduce the absorption of hydrogen chemically associated with the zirconium in the cladding.

These 4 m-long cladding tubes, with a nominal wall thickness of 570 $\mu$m and a nominal external diameter of 9.5 mm, have been shown to be much more resistant to oxidation when coated with a 10–20 $\mu$m-thick layer of chromium (Cr) on their outer surface,[1] both under nominal reactor operating conditions and in hypothetical accident situations. In addition to improved resistance to oxidation, it appears that this Cr coating protects the cladding from diffusion of oxygen within the underlying M5 substrate. Exposing the Cr/M5 bilayer to 1100 °C steam for 12 000 s revealed very low oxidation kinetics.[2,3] Before being put into service, this Cr layer requires non-destructive characterization, especially in terms of thickness and uniformity of the coating. The most used non-destructive techniques are eddy current and ultrasound. However, ultrasound techniques are preferred because eddy current techniques do not provide local measurements. In conventional ultrasonic techniques, the generation and the detection are generally achieved with piezoelectric transducers, which requires fluid coupling. One solution to avoid this problem is to use non-contact laser ultrasonic (LUS) techniques, which also provide the advantage of a broad bandwidth. LUS techniques have been used by Yeh and Yang[4] and Liu and Yang[5] to characterize isotropic zirconium alloy $Z_R$ –4 cladding tubes. They measured axial and circumferential guided waves to evaluate the tube average thickness and elastic moduli and also assess the effect of hydrogen charging. In parallel, Cès *et al.*[6] observed zero group velocity Lamb mode resonances, generated by laser line sources of different orientations in similar tubes. These measurements provided a local estimation of the thickness and revealed the elastic anisotropy of the $Z_R$ –4 alloy. The elastic constants of this material were evaluated assuming transverse isotropy. These two studies demonstrated the value of LUS for assessing the elastic properties of cladding tubes.

In this paper, we study the impact of a Cr coating on the elastic guided waves propagating in M5 cladding tubes.

a)Email: hafsa.diboune@espci.fr

 

https://doi.org/10.1121/10.0042186

Modes with energy concentrated near the outer surface are expected to be the most sensitive to the coating. Surface waves propagating in a layer deposited on a semi-infinite substrate has been the object of extensive studies more than 50 years ago.[7,8] Two cases are often distinguished: "slow-on-fast" (or "loading") and "fast-on-slow" (or "stiffening"), depending on whether the shear velocity of the coating is much smaller than the shear velocity of the substrate, and *vice versa*. The dispersion of waves of both cases was measured using the angle-dependent acoustic reflectivity of water-embedded coated substrates.[9]

Later on, it was shown that LUS techniques are well suited to study these waves, and many experimental results have been reported in the literature. The dispersion of pseudo-surface waves was measured on a coated semi-infinite substrate being either isotropic[10,11] or anisotropic.[12] This dispersion can be exploited to evaluate properties of the coating, such as thickness or bulk velocities. For example, Bescond *et al.*[13] proposed *in situ* simultaneous measurement of thickness, elastic moduli, and density of thermal sprayed tungsten carbide-cobalt (WC-Co) alloy coating on steel, while Jenot *et al.*[14] controlled gold coatings on silicon wafers. These two studies investigate the slow-on-fast case, where the surface wave velocity decays from the Rayleigh velocity of the substrate to the Rayleigh velocity of the coating as frequency increases.

Fast-on-slow cases were also investigated for different degrees of stiffening using laser generation. Schneider *et al.*,[15] for instance, focused on the control of titanium nitride (TiN) coated steel. They have also measured the dispersion of surface acoustic waves to determine the Young's modulus of thin films ($< 50$ nm) and multilayer materials [diamond-like carbon and aluminum on steel and (100) silicon].[16] Watzl *et al.*[17] proposed a single-shot measurement of the surface wave to characterize a bilayer aluminum alloy plate and they have also investigated a highly dissipative copper-clad epoxy laminate.

In this contribution, we investigate the mode repulsion phenomena induced by the "strong stiffening" of the Cr coating on a finite M5 substrate. We determine which modes are both sensitive to the coating and well observed by LUS technique. To this end, we use a simple yet effective model together with experimental validations. In Sec. II, we first propose a full evaluation of the M5 effective elastic parameters that will then be used for the modelization. In Sec. III, surface waves propagating along a Cr coating on an infinite M5 substrate are described. Then, we investigate the variations induced by the Cr layer on the second longitudinal mode. The link with surface modes in the case of an infinite substrate is discussed. Section IV is dedicated to the study of longitudinal modes in tubes. We first propose a simplified model to determine which modes are best measured by the LUS. The relation between these measured modes and the leaky surface modes for a coated semi-infinite substrate is then highlighted. Experimental dispersion curves and their dependence on the coating thickness are finally presented.

## II. M5 EFFECTIVE ELASTIC PARAMETERS

To characterize the Cr layer with guided waves, it is first necessary to evaluate the elastic properties of the M5 substrate. To this end, the grain orientation distribution is measured by x-ray diffractometry and the effective M5 elastic tensor is estimated by homogenization. Guided waves are then measured with a LUS setup and their dispersion curves are compared to the theoretical ones calculated with the open-source software `GEWtool`[18] using the previously estimated stiffness tensor.

### A. X-ray diffractometry to estimate the M5 elastic tensor

The x-ray diffractometry technique is based on the interaction of x rays with the atomic lattice of a crystal. The x rays reflecting of two different crystal planes must interfere constructively to form a maximum of intensity.[19] This measurement provides the orientation distribution function (ODF) defined as the fraction of grains with a particular orientation.[20]

The effective elastic constants of the M5 polycrystal are obtained from those of the zirconium single crystal[21] and the ODF (cladding sample). Using crystal lattice orientations $g$, the ODF $f(g)$ is generally expressed, in the form of the Euler angles $\varphi_1$, $\Phi$, and $\varphi_2$. For a microstructure containing grains with different orientations, the ODF is defined by the following formula:

$$\frac{dV}{V} = f(g)\,dg \quad \text{with} \quad dg = \frac{1}{8\pi^2}\sin\Phi\, d\varphi_1\, d\Phi\, d\varphi_2, \tag{1}$$

$$\int f(g)\,dg = 1, \tag{2}$$

where $V$ is the volume of the sample and $dV$ is the volume of crystallites with the orientation $g$ within the angular element $dg$. To calculate the elasticity tensor from the ODF, the relations proposed for hexagonal materials by Li and Thompson[22] were used, here extended to non-orthotropic materials. This calculation relies on the well-known Voigt and Reuss approximations, which provide the upper and lower bounds of the elastic properties.[23] The effective elastic tensor obtained from these approximations is given in Table I in Appendix A. The relative distance between the Reuss and Voigt tensors $||C_R - C_V||/||C_V||$, where $||||$ is the Frobenius norm, is less than 1%, meaning that these tensors are very close. In the following, we choose to use the arithmetic average of the Voigt and Reuss approximations, called the Hill approximation, which has often been shown to be very close to the experimental values.[24]

The elastic anisotropy of the M5 alloy can be quantified using the universal elastic anisotropy index $A^U$ introduced by Ranganathan and Ostoja-Starzewski in 2008.[25] Unlike the Zener index defined for cubic materials only, this index applies to any type of anisotropy. It is equal to zero for isotropic media and can reach the value of 9 for highly anisotropic crystals and even 15 for composites. For the M5

alloy, it is $A^U = 0.009$, which corresponds to a weak anisotropy. However, considering all propagation directions, the minimal and maximal shear wave velocities are, respectively, 2290 and 2412.3 m/s (obtained with an M5 density $\rho = 6650$ kg/m$^3$). This 5% variation has an impact on the measured guided waves and needs to be taken into account in the model.

### B. Guided wave measurements with laser ultrasound

Elastic guided waves are measured along the tube using a LUS setup (Fig. 1). Their generation is achieved with an neodymium-doped yttrium aluminum garnet (Nd:YAG) pulsed laser with a pulse duration of $\sim 8$ ns, providing a wide bandwidth. The laser beam is focused on a line source using a cylindrical lens with 100 mm focal length. The linewidth, measured using the knife-edge technique and assuming a Gaussian profile, is equal to 200 $\mu$m at $1/e$. The deposited energy ($E = 3$ mJ per pulse) is kept below the melting threshold of the material in order to be non-destructive. The out-of-plane displacement is measured with a homodyne interferometer. Exploiting the reciprocity principle, the wavefield $u(z,t)$ is recorded by scanning the source along the tube axis $\mathbf{e}_z$ over 20 mm with a 20 $\mu$m pitch and a 25 $\mu$s acquisition duration [Fig. 2(a)].

The dispersion curves $U(k,\omega)$ are obtained by a spatio-temporal Fourier transform of the displacement field $u(z,t)$ after spatial apodization with a Blackman window. As observed in Fig. 2(b), several modes are well measured. The slowest mode at the bottom right corner is the pressure wave propagating at the speed of sound and is due to the heating of the air caused by the laser impact. The other modes are the (quasi)longitudinal modes, denoted $L_n$, with $n$ being the mode order, as already observed by Cès *et al.*[6] The line source favors these modes that are analogous to Lamb waves in plates as the ratio between the tube's thickness and diameter is small ($0.570/9.5 \ll 1$). Note that the anisotropy of the material couples the longitudinal modes $L_n$ to the torsional modes $T_n$ but we neglect this effect because it is very small (see Appendix B). Considering that the line source, about 8 mm long, covers slightly more than a quarter of the tube's circumference, it is expected that the flexural modes $F(m,n)$ of circumferential orders m $\leqslant 2$ are also generated. As also illustrated in Appendix B, the tube wall being thin, the dispersion curves of these modes barely differ from the dispersion curves of longitudinal modes $L_n$ and torsional modes $T_n$ (Fig. 10). For wavenumbers measured with our setup (k $\geqslant 2$ rad/mm), the $F(m,n)$ modes are superimposed on torsional and longitudinal modes. However, torsional modes have zero out-of-plane displacements and they are not detected by the interferometer. Therefore, the measured modes are well described by only the longitudinal modes $L_n$.

Using the elastic constants determined in Sec. II, the longitudinal modes are calculated with the `GEWtool`.[18] This flexible open-source software implements a semi-analytical approach, based on spectral elements,[26] to efficiently and reliably compute the waveguide modes.[27–30] The agreement between the theoretical and experimental curves displayed in Fig. 2 being very good, we consider that the

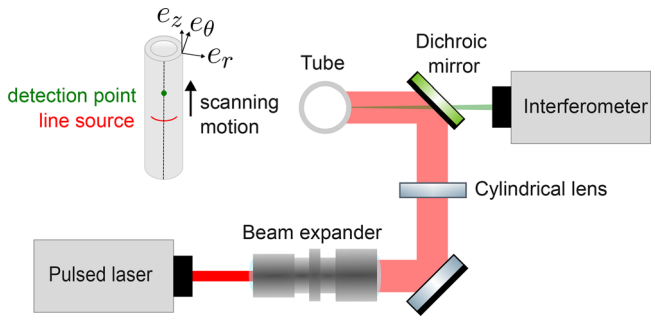


FIG. 1. Laser ultrasound experimental setup.

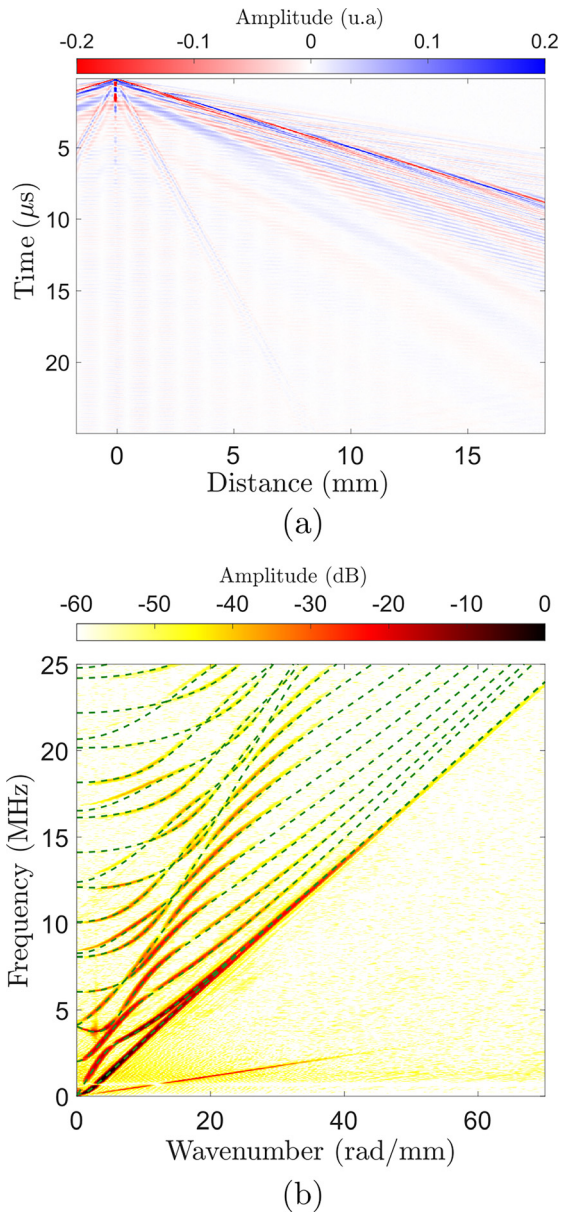


FIG. 2. (a) B-scan of the axial guided modes displacement and (b) spatio-temporal Fourier transform of the displacement field measured along an M5 cladding tube and theoretical dispersion curves of the $L_n$ modes (dashed line).

https://doi.org/10.1121/10.0042186

estimation of the elastic tensor by x-ray diffractometry is precise enough to accurately describe the elastic behavior of the M5 alloy in the studied frequency range.

Like the $A_0$ and $S_0$ modes in plates, for increasing frequencies, the two first longitudinal modes $L_1$ and $L_2$ of the M5 tube converge toward a combination of Rayleigh surface waves inside and outside the tube, as can be seen in Fig. 2. In the following, we will see that the coating on the outside of the tube suppresses this convergence to a common velocity, as it breaks the symmetry.

## III. THEORY OF GUIDED MODES IN CR COATINGS

We now consider Cr coatings on the M5 substrate. The Cr is assumed isotropic with elastic properties taken from literature.[31] The bulk wave velocities and the densities of both materials are summarized in Table II. As the Cr shear velocity (4005 m/s) is much larger than the maximum possible shear velocity of the M5 (2412 m/s), the first two longitudinal modes $L_1$ and $L_2$ are greatly modified by the coating. Like for Lamb waves in plates, the slowest mode $L_1$ is expected to converge toward the slowest surface mode concentrated on the uncoated surface inside the tube while the $L_2$ mode is expected to be faster and concentrated on the outer surface of the tube. To understand the impact of the layer on the $L_2$ mode, we first recall the theory of surface waves for a fast layer deposited on a slow infinite substrate, the so-called fast-on-slow case.

### A. Chromium layer on infinite substrate

Since the pioneering studies of Tiersten[7] in 1969, it is well known that a coating modifies the surface modes of a semi-infinite substrate in a way that mostly depends on the frequency and on the ratio of its shear wave velocity $V'_T$ to that of the substrate $V_T$.

If $V'_T/V_T > \sqrt{2}$, as is the case for a Cr/M5 bilayer, the layer stiffens the substrate and increases the surface wave velocity beyond that of the substrate alone. Furthermore, as shown by Farnell and Adler,[8] this surface wave exists only below a given cut-off frequency. In this case, also referred to as strong stiffening, a surface acoustic wave (SAW) propagates with a velocity that increases from the Rayleigh velocity at zero frequency to the shear velocity of the substrate at the cut-off frequency. Above this cut-off frequency, all modes are leaky and radiate energy into the substrate.

We compute the SAW and leaky modes by a semi-analytical method, which leads to a nonlinear eigenvalue problem. Solution methods exist only for isotropic half-spaces and, in the following analysis, we therefore use an isotropic M5 stiffness tensor. This tensor is obtained by averaging the Hill M5 tensor provided in Appendix A (Table I) uniformly over all propagation directions. The nonlinear eigenvalue problem is then solved with a very robust method, akin to Refs. 32 and 33, while modes are selected as proposed in Ref. 34. The leaky wave with the lowest radiation damping and the unattenuated SAW are displayed in Fig. 3 (dashed lines). Our computation confirms

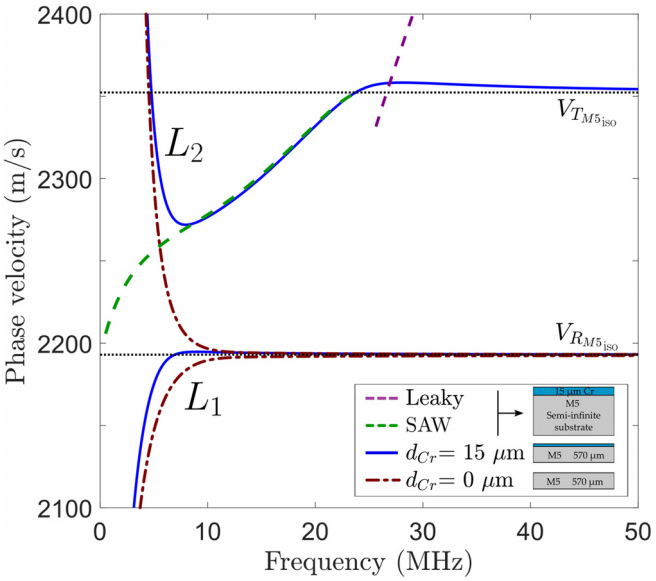


FIG. 3. Phase velocity of surface and leaky waves of a 15 $\mu$m-thick Cr coating on infinite M5 substrate (dashed lines) compared to the $L_1$ and $L_2$ modes in the coated (solid blue) and uncoated tube (dashed brown). All modes are calculated using the isotropic M5 stiffness tensor.

that the SAW velocity (green) ranges from the Rayleigh velocity of the substrate at zero frequency to the shear velocity of the substrate at the cut-off frequency and that this cut-off occurs at around 23 MHz for a 15 $\mu$m-thick Cr coating. Above this frequency, only leaky modes exist. The importance of the first leaky mode will be highlighted in Sec. III B.

### B. Cr layer on cladding tube

In the Cr coated tube, due to the finite thickness of the substrate, the effect of the deposited layer is even more complex: a coupling between the "Lamb type" guided modes and the surface modes appears. In Fig. 3, we plotted the $L_1$ and $L_2$ modes for both the uncoated and the coated tubes using the isotropic M5 stiffness tensor. We observed that the $L_1$ mode is only slightly modified by the coating. As expected, for both cases, this mode converges to the Rayleigh mode of the M5 substrate. Conversely, the $L_2$ mode is significantly modified when the coating is present. In the medium frequency range, from 8 to 23 MHz, this mode overlaps the SAW of the Cr coated semi-infinite M5 substrate. Consequently, in this frequency range, the mode is similar to a surface mode and should be very sensitive to the coating. Furthermore, for higher frequencies, its velocity converges to the substrate shear velocity instead of the Rayleigh wave. Above 23 MHz, this mode is no longer sensitive to the Cr layer thickness.

To confirm this point, we now study the dependence of the $L_2$ mode's phase velocity on the thicknesses of both the Cr and the M5 in Fig. 4. The $L_2$ mode calculated for five coating thicknesses $d_{Cr}$ ranging from 5 to 30 $\mu$m with an M5 thickness of 570 $\mu$m is compared to five $d_{M5}$ evolving from 550 to 590 $\mu$m with $d_{Cr} = 15$ $\mu$m. The phase velocity of $L_2$

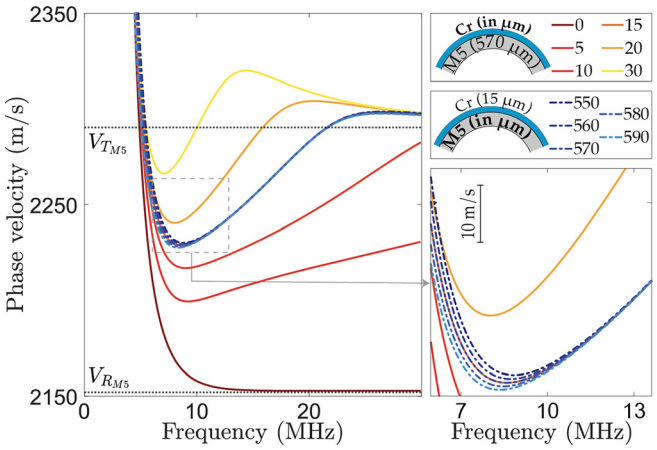


FIG. 4. Phase velocity of the $L_2$ mode for different M5 (dashed lines) substrate thicknesses (with $d_{Cr}$= 15 $\mu$m) and different Cr thicknesses (solid lines) with $d_{M5}$= 570 $\mu$m.

is very sensitive to the Cr coating thickness. For $d_{Cr} = 15\,\mu$m, this sensitivity is maximal in the frequency range of 8–20 MHz, whereas it barely depends on the M5 thickness. This mode appears as an interesting candidate for Cr thickness estimation. However, an important question is whether this mode can always be observed with LUS. In Sec. IV A, using a simple model, we show that, depending on the frequency, the best observed mode is not necessarily the $L_2$ mode.

## IV. LUS MEASUREMENTS OF LONGITUDINAL MODES

The guided modes that are well measured depend on the chosen experimental technique. Laser generation of elastic waves by thermoelastic expansion of metals was modeled in detail in Refs. 35–38. In Sec. IV A, a simplified model to describe the measurement of guided modes achieved with our experimental setup is presented.

### A. Theoretical observability

We define the *observability* $O$ of a mode as the combined efficiency of excitation and detection. The laser source is focused onto a finite line along the tube's circumference and operates in the thermoelastic regime. The pulse leads to a sudden thermal expansion that remains for a long time due to the relatively slow thermal diffusion process. As the laser absorption length is only a few nanometers in depth, the source is concentrated at the surface. Furthermore, as the line source is thin, the shear stress component $\tau_{rz}$ is dominant.[39] Concerning the detection, the laser interferometer is sensitive to the normal surface displacement. Under these conditions, we demonstrate in Appendix C that the wave's observability can be inferred from the modal solutions ($\mathbf{u}$, $k$, $\omega$). In the case of axial waves in a tube, this observability follows:

$$O = \frac{|k|}{4\overline{P}}\,|u_z(r_o)|\,|u_r(r_o)|, \tag{3}$$

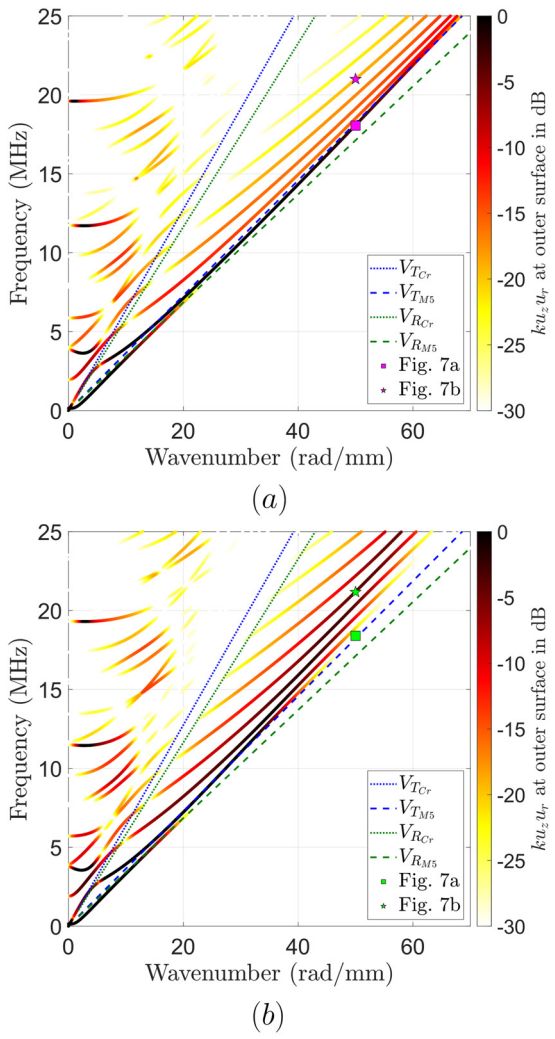


FIG. 5. Observability of the longitudinal modes for (a) 15 $\mu$m-thick and (b) 31 $\mu$m-thick Cr coatings. The shear and Rayleigh waves are indicated in blue and green lines, respectively, for both materials.

where $\overline{P}$ is the total average power flux, $r_o$ is the outer radius of the tube, and $u_z$ and $u_r$ are the mode's axial and radial displacement components, respectively.

The observabilities calculated for M5 tubes coated by a 15 $\mu$m or by a 31 $\mu$m-thick Cr layer are represented in Figs. 5(a) and 5(b), respectively. They confirm that the $L_1$ mode is not observed at high wavenumbers, as it becomes a Rayleigh wave on the inner surface of the tube. The observability of the $L_2$ mode is strongly diminished above 20 MHz while its phase velocity converges to the M5 shear velocity. Above a given frequency, higher-order modes are better observed than the $L_2$ mode. This effect can be understood by referring to the leaky mode of a similar Cr layer deposited on a semi-infinite M5 substrate. Indeed, as can be observed in the phase velocity curves displayed in Fig. 6, the region where higher-order modes of the finite bilayer have a high observability follows the dispersion curve of the leaky mode (dashed magenta line) in the infinite bilayer.

To illustrate this observability issue, it is instructive to compare the displacement profiles of the modes. The axial

https://doi.org/10.1121/10.0042186

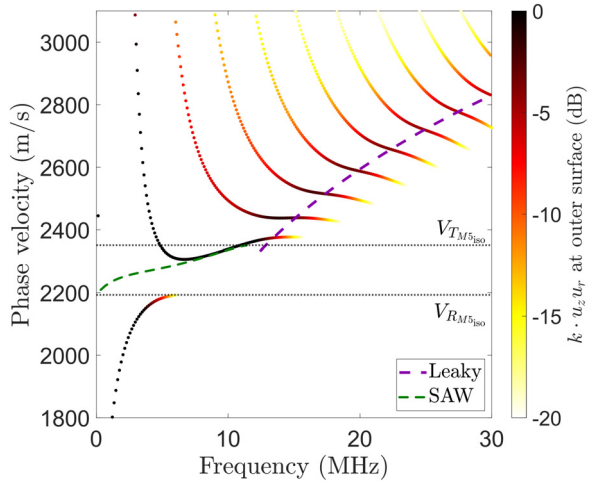


FIG. 6. Phase velocities of the SAW (green) and leaky (purple) modes for a Cr layer on an infinite M5 substrate compared to the phase velocities of the longitudinal waves in a Cr coated M5 tube plotted with color-coded observabilities. $d_{Cr} = 31\ \mu$m. All modes are calculated using the isotropic M5 stiffness tensor.

and radial components of the displacements of the $L_2$ and $L_6$ modes at $k = 50$ rad/mm are displayed in Fig. 7. For $d_{Cr} = 15\ \mu$m, both components of the displacements of the $L_2$ mode [Fig. 7(a)] are large at the surface and decay through the thickness in a similar manner to a surface wave, whereas the $L_6$ mode [Fig. 7(b)] is uniformly distributed through thickness. In contrast to this, with $d_{Cr} = 31\ \mu$m, the $L_2$ mode's [Fig. 7(c)] displacement components dominate in the substrate, whereas the displacement components of the $L_6$ mode [Fig. 7(d)] are larger near the surface than in the substrate. This explains why the latter is well detected.

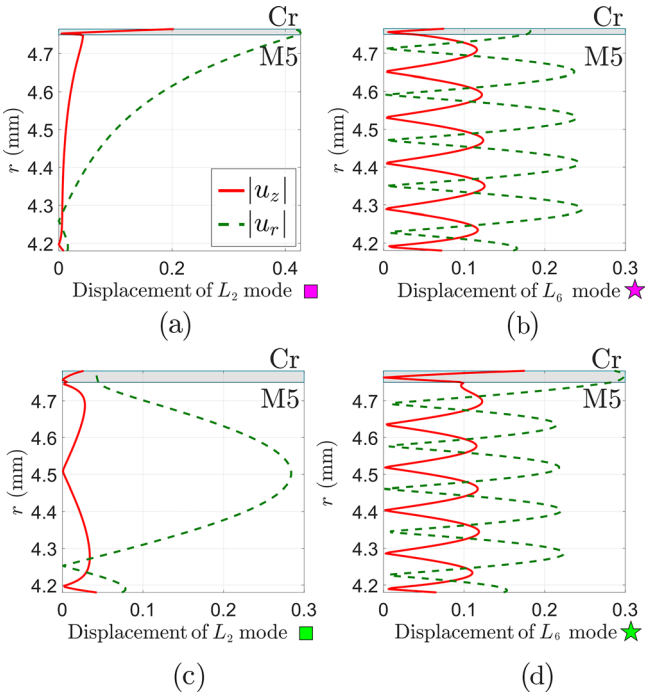


FIG. 7. In-plane ($u_z$) and out-of-plane ($u_r$) displacements of the (a) and (c) $L_2$ mode, (b) and (d) $L_6$ mode at $k = 50$ rad/mm for (a) and (b) 15 $\mu$m-thick Cr coating and (c) and (d) 31 $\mu$m-thick coating.

## B. Experimental results

LUS measurements were done on samples of M5 tubes coated with Cr by physical vapor deposition. Destructive measurements were performed on both ends of each sample using the ball-cratering method to assess the uniformity of the protective coating. This method ensures a thickness measurement precision of 0.8 $\mu$m. Following the method described in Sec. II B, the dispersion was measured on Cr/M5 tubes with 15 $\mu$m- and 31 $\mu$m-thick Cr coatings (see Fig. 8). A Blackman window was applied in the spatial domain before the spatio-temporal Fourier transform. Figure 8(b) shows that for a 31 $\mu$m-thick coating, the $L_2$ mode is almost no longer measured from 45 rad/mm upwards, in benefit of higher-order modes, as predicted in Fig. 5. For a lower coating thickness (15 $\mu$m), the $L_2$ is the predominant surface mode up to k = 70 rad/mm. These results confirm the theoretical prediction in Sec. IV A. Lastly, to illustrate the typical fast-on-slow dispersion of the surface mode, a waveform is shown and discussed in Appendix D.

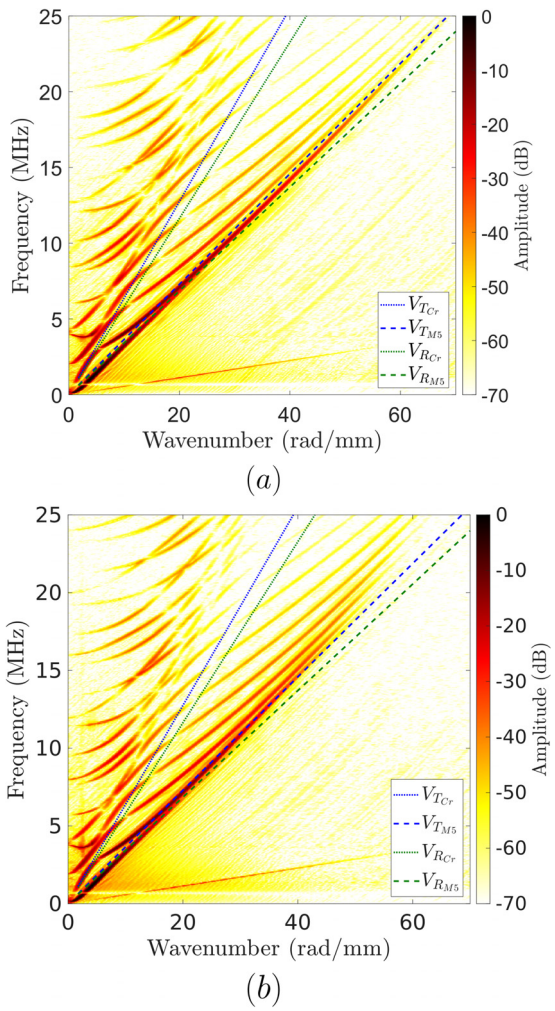


FIG. 8. Experimental dispersion curves for (a) 15 $\mu$m and (b) 31 $\mu$m-thick Cr layers. Shear and Rayleigh velocities are indicated in blue and green lines, respectively, for both materials.

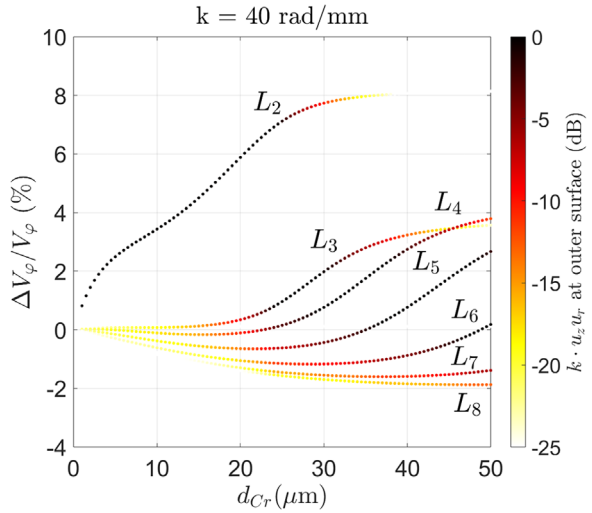


FIG. 9. Relative phase velocity change of longitudinal surface modes as a function of Cr thickness for the modes $L_n$ with $n$ varying from 2 to 8, with color-coded observability.

### C. Sensitivity of measured modes to the Cr coating

The observability calculated for the Cr coated tubes (Sec. IV A), which agrees well with the measurements, reveals that higher-order modes can better be detected than the $L_2$ mode, depending on the layer thickness and frequency. Therefore, for the purpose of characterization, it is useful to evaluate the sensitivity of these higher-order modes to Cr thickness changes. To this end, the relative phase velocity changes $\Delta V_\varphi/V_\varphi$ of the longitudinal modes $L_n$—for $n = 2$ to 7—are calculated at a fixed wavenumber as a function of the layer thickness $d_{Cr}$. They are displayed for $k = 40$ rad/mm in Fig. 9, with color-coded observabilities. It appears that the $L_2$ mode has the highest relative velocity change, which first increases significantly with the Cr thickness, then reaches a plateau for $d_{Cr} > 25\ \mu$m as the observability drops. For larger thicknesses, higher-order modes have larger observability and appear to be more sensitive to thickness variations. Thus, the $L_2$ mode is appropriate to evaluate the chromium thickness up to 25 $\mu$m. At higher frequencies, the task is much more complicated due to the multitude of sensitive modes.

## V. CONCLUSION

A study of laser generated surface waves in Cr coated M5 tubes is presented. It is shown that the dispersion and observability of the longitudinal mode $L_2$ significantly depends on the Cr layer. The theoretical observability curves, calculated with a proposed simplified model, are in good qualitative agreement with experimental results. The phase velocity of this mode is highly sensitive to the Cr coating thickness while remaining unaffected by variations in the M5 substrate thickness. As frequency increases, the observability of the $L_2$ drops while those of higher-order longitudinal modes increases. This effect, depending on the Cr layer thickness, indicates the potential of higher-order modes to characterize thicker coatings. In addition, the coincidence between the observability domain of the $L_2$ mode and the SAW for a similar layer on an infinite substrate is shown. The relation between leaky modes and the observability domain of higher-order longitudinal modes is also highlighted. For these observations, the experimental dispersion curves align well with theoretical ones calculated with `GEWtool`. This study confirms the potential of non-contact LUS techniques for the characterization of thin coatings on nuclear fuel cladding tubes.

## ACKNOWLEDGMENTS

This work has received partial support under the program "Investissements d'Avenir" launched by the French Government under Reference No. ANR-10-LABX-24. M5 and M5Framatome are trademarks or registered trademarks of Framatome or its affiliates, in the USA or other countries.

## AUTHOR DECLARATIONS

### Conflict of interest

The authors have no conflicts to disclose.

## DATA AVAILABILITY

The data that support the findings of this study are available from the corresponding author upon reasonable request.

## APPENDIX A: M5 ALLOY ELASTIC PARAMETERS

The polycrystalline elastic tensors of the M5 uncoated tube, obtained from x-ray diffraction measurements and estimated using the Voigt and Reuss approximations, are given below.

TABLE I. Voigt, Reuss, and Hill elastic constants $C_{ij}$ of M5 deduced from x-ray diffractometry and isotropic M5 constants (in GPa).

| | Voigt | Reuss | Hill | Isotropic |
|---|---|---|---|---|
| $C_{11}$ | 142.85 | 142.46 | 142.65 | 143.65 |
| $C_{12}$ | 70.10 | 70.43 | 70.26 | 71.16 |
| $C_{13}$ | 69.37 | 69.9 | 69.635 | 71.16 |
| $C_{22}$ | 145 | 143.62 | 144.31 | 143.65 |
| $C_{23}$ | 71.76 | 72.27 | 72.01 | 71.16 |
| $C_{33}$ | 148.18 | 146.08 | 147.13 | 143.65 |
| $C_{44}$ | 38.26 | 37.96 | 38.11 | 36.25 |
| $C_{55}$ | 34.49 | 34.9 | 34.69 | 36.25 |
| $C_{66}$ | 34.47 | 34.26 | 34.36 | 36.25 |

TABLE II. Bulk velocities and densities of chromium (Cr), M5, and isotropized M5 materials. The minimum and maximum velocities over all directions are given for the anisotropic M5 for the sake of reference.

| | $\rho$ (kg/m$^3$) | $V_L$ (m/s) | $V_T$ (m/s) |
|---|---|---|---|
| Cr | 7194 | 6608 | 4005 |
| M5 | 6650 | Min 4642 | Min 2290 |
| | | Max 4744 | Max 2412 |
| $M5_{iso}$ | 6650 | 4682 | 2351 |

https://doi.org/10.1121/10.0042186

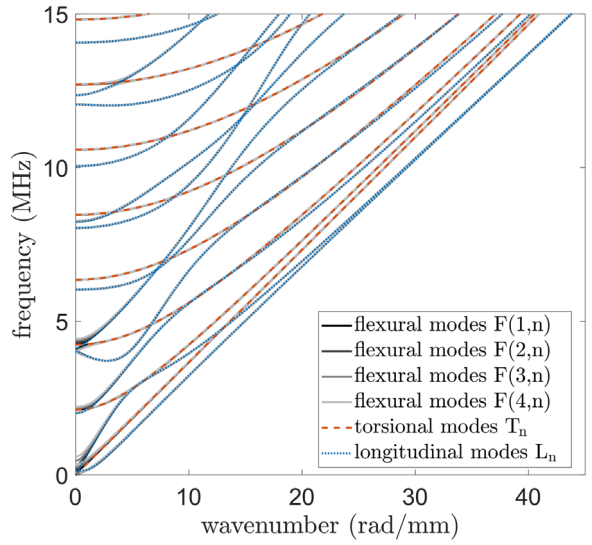


FIG. 10. Dispersion curves of the longitudinal $L_n$ and torsional $T_n$ guided modes compared to those of the flexural modes $F(m,n)$, of low circumferential orders ($m=1,..,4$) in a 570 $\mu$m-thick M5 tube. The mode families coincide except at small wavenumbers and low frequencies.

## APPENDIX B: GUIDED MODES IN AN M5 TUBE

Modes propagating in a tube are generally denoted $F(m,n)$, $m$ being the order along the circumference, and $n$ the through-thickness order. The $F(0,n)$ modes have uniform displacement distribution along the circumference. In isotropic media, they segregate into longitudinal modes, denoted $L_n$, and torsional ones, denoted $T_n$. Due to the M5 anisotropy, $L_n$ and $T_n$ modes are coupled in our sample. However, this coupling is very weak and has been neglected for the computation of dispersion curves. Figure 10 shows dispersion curves of guided modes propagating in an M5 cladding tube of 570 $\mu$m thickness and 9.5 mm outer diameter. The five lowest circumferential orders $m$ are included. For increasing orders, differences appear for small wavenumbers near the first two cut-off frequencies; it is clear that up to the fourth order, the modes are superimposed in the range of frequency-wavenumber of interest in our study. For this reason, only longitudinal modes are discussed in the paper, as torsional ones are not measured by our system.

## APPENDIX C: OBSERVABILITY CALCULATION

We define the *observability* $O$ of a given mode as the relative magnitude expected to be acquired by the measurement system. For simplicity, we derive it for a plate geometry as seen in Fig. 11. The interferometer's output signal is proportional to the out-of-plane displacement magnitude $|u_z(h)|$ at the surface $z=h$. If $\mathbf{u}(z)$ denotes the modal displacement eigenfunction and $A(k,\omega)$ is the modal amplitude excited by the source, the observability of mode $(\mathbf{u},k,\omega)$ can be defined as

$$O = |A(k,\omega)||u_z(h)|. \tag{C1}$$

We further need to determine the mode's amplitude $A(k,\omega)$ from the spatiotemporal traction $\boldsymbol{\tau}(x,t)$ that is generated by the pulsed laser source. It can be regarded as a spontaneous thermoelastic dilatation concentrated at the surface. This means that, neglecting thermal diffusion, the acoustic source behaves in time as a Heaviside step function $H(t)$. Furthermore, we consider an idealized dipole line generating only shear tractions on the plate's surface at $z=h$. The unit surface traction is then[35–37]

$$\boldsymbol{\tau}(x,t) = H(t)\delta'(x)\mathbf{e}_x, \tag{C2}$$

where $\delta'$ denotes the $x$-derivative of the Dirac delta function.

With the tractions $\boldsymbol{\tau}$, it is possible to compute the modal amplitude $A$, thanks to the complex orthogonality relation between waveguide modes established by Auld and Kino,[40] Kino,[41] and Auld.[42] For a complete derivation, see Appendix E in Ref. 41. The overall result, given in Ref. 42 by Eq. (10.134), is that the mode's spatiotemporal axial wave field $\tilde{a}(x,t)$ is governed by

$$4\overline{P}[\partial_x\tilde{a} - \mathrm{i}k\tilde{a}] = \mathbf{v}^*(h)\cdot\boldsymbol{\tau}(x,t), \tag{C3}$$

where we use the particle velocity $\mathbf{v} = -\mathrm{i}\omega\mathbf{u}$ and the total average power flux $\overline{P}$ of the mode. The latter can be computed given the stiffness tensor $\mathbf{c}$ as

$$\overline{P} = \int_{-h}^{h} \frac{1}{2}\left|\mathrm{Re}\left\{\mathbf{v}^*\cdot\mathbf{c} : (\mathrm{i}k\mathbf{e}_x + \partial_z\mathbf{e}_z)\mathbf{u}\right\}\right| \mathrm{d}z. \tag{C4}$$

From Eq. (C3), we find that the governing differential equation for the envelope $\tilde{A}(x,t) = \tilde{a}(x,t)\mathrm{e}^{-\mathrm{i}kx}$, i.e., the part without the harmonic modulation, is

$$\partial_x\tilde{A}(x,t) = \frac{1}{4\overline{P}}\mathbf{v}^*(h)\cdot\boldsymbol{\tau}(x,t)\mathrm{e}^{-\mathrm{i}kx}. \tag{C5}$$

Its general solution reads

$$\tilde{A}(x,t) = \frac{1}{4\overline{P}}\mathbf{v}^*(h)\cdot\int_{-\infty}^{x}\boldsymbol{\tau}(\xi,t)\mathrm{e}^{-\mathrm{i}k\xi}\,\mathrm{d}\xi. \tag{C6}$$

As we are interested in the amplitude outside the source region, i.e., where $\boldsymbol{\tau}=0$, we can choose $x\to\infty$. In that case, the integral is recognized as the Fourier transform $\mathcal{F}_x$ and results in a dependence on $k$. To obtain the frequency dependence, we additionally perform the temporal Fourier transform $\mathcal{F}_t$. This yields the amplitude in the spectral domain

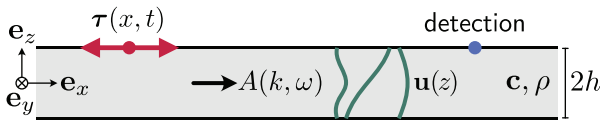


FIG. 11. Sketch of the cross sectional plate geometry. The traction $\boldsymbol{\tau}$ acts on an infinite line along $y$ and generates the mode $(\mathbf{u}(z),k,\omega)$ with amplitude $A$ that propagates to the detection point.

$$A(k,\omega) = \frac{1}{4\overline{P}}\mathbf{v}^*(h)\cdot\mathcal{F}_x\mathcal{F}_t\boldsymbol{\tau}(x,t). \tag{C7}$$

Finally, we insert the assumed tractions from Eq. (C2) into Eq. (C7). The Fourier transforms of $H(t)$ and $\delta'(x)$ exist in the sense of distributions and are $\mathcal{F}_x\delta'(x) = \mathrm{i}k$ and p.v. $\mathcal{F}_t H(t) = -1/\mathrm{i}\omega$. Considering this, the modal amplitude becomes

$$A = -\frac{1}{4\overline{P}}\frac{\mathrm{i}k}{\mathrm{i}\omega}v_x^*(h). \tag{C8}$$

Hence, the observability [Eq. (C1)] with an ideal laser line source is

$$O = \frac{|k|}{4\overline{P}}|u_x(h)||u_z(h)|. \tag{C9}$$

Note that Eq. (C7) is an exact far-field theory for surface sources but Eq. (C9) is an approximation due to the strong idealization of the source given in Eq. (C2). The theory extends to axial waves in tubes and the equivalent in cylindrical coordinates is given in Eq. (3).

## APPENDIX D: ILLUSTRATION OF THE STIFFENING EFFECT

The M5 layer of the cladding tubes is relatively thin. For this reason, there are many guided modes that are measured simultaneously, thanks to the large bandwidth of our experimental setup. To visualize the fast-on-slow dispersive surface wave, a time trace measured on the tube with a 15 $\mu$m Cr coating at a distance of 10.1 mm from the source is shown in Fig. 12(a). The signal is difficult to interpret because the multitude of modes mostly overlaps in the temporal domain. However, from Fig. 3, we know that above 8 MHz, the $L_2$ mode becomes a surface mode and the amplitude of other modes is about 10 dB lower in the measurements, as can be seen in Fig. 8(a). Therefore, by applying a high-pass filter to suppress modes below 8 MHz, it is possible to better visualize the contribution of the $L_2$ mode [see Fig. 12(b)]. The fast-on-slow dispersion effect is then clearly seen between 4.5 and 5.5 $\mu$s.

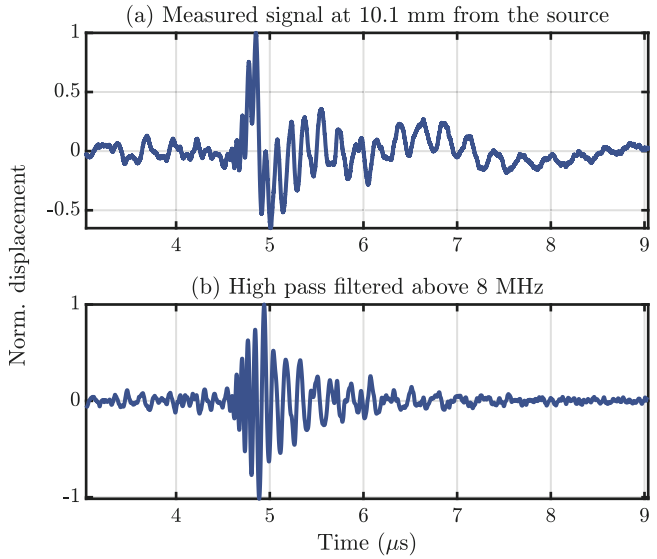


FIG. 12. (a) Measured time trace at 10.1 mm from the source, (b) high-pass filtered signal.

[1]D. V. Nguyen, M. Le Saux, L. Gélébart, J.-C. Brachet, J.-P. Bonthonneau, A. Courcelle, R. Guillou, E. Rouesne, and S. Urvoy, "Mechanical behavior of a chromium coating on a zirconium alloy substrate at room temperature," J. Nucl. Mater. **558**, 153332 (2022).
[2]J. Bischoff, C. Delafoy, C. Vauglin, P. Barberis, C. Roubeyrie, D. Perche, D. Duthoo, F. Schuster, J.-C. Brachet, E. W. Schweitzer, and K. Nimishakavi, "AREVA NP's enhanced accident-tolerant fuel developments: Focus on Cr-coated M5 cladding," Nucl. Eng. Technol. **50**(2), 223–228 (2018).
[3]M. L. Saux, V. Vandenberghe, P. Crébier, J.-C. Brachet, D. Gilbon, J.-P. Mardon, A. Cabrera, and P. Jacques, "Influence of steam pressure on the high temperature oxidation and post-cooling mechanical properties of Zircaloy-4 and M5 cladding (LOCA conditions)," in *Zirconium in the Nuclear Industry: 17th International Symposium ASTM STP 1543*, Hyderabad, India (February 2013), pp.1002–1053 (2014).
[4]C.-H. Yeh and C.-H. Yang, "Characterization of mechanical and geometrical properties of a tube with axial and circumferential guided waves," Ultrasonics **51**(4), 472–479 (2011).
[5]I.-H. Liu and C.-H. Yang, "A novel procedure employing laser ultrasound technique and simplex algorism for the characterization of mechanical and geometrical properties in Zircaloy tubes with different levels of hydrogen charging," J. Nucl. Mater. **408**(1), 96–101 (2011).
[6]M. Cès, D. Royer, and C. Prada, "Characterization of mechanical properties of a hollow cylinder with zero group velocity Lamb modes," J. Acoust. Soc. Am. **132**(1), 180–185 (2012).
[7]H. F. Tiersten, "Elastic surface waves guided by thin films," J. Appl. Phys. **40**(2), 770–789 (1969).
[8]G. Farnell and E. Adler, "Elastic wave propagation in thin layers," Phys. Acoust. **9**, 35–127 (1972).
[9]A. H. Nayfeh and D. E. Chimenti, "Reflection of finite acoustic beams from loaded and stiffened half-spaces," J. Acoust. Soc. Am. **75**(5), 1360–1368 (1984).
[10]D. Schneider, T. Schwarz, and B. Schultrich, "Determination of elastic modulus and thickness of surface layers by ultrasonic surface waves," Thin Solid Films **219**(1), 92–102 (1992).
[11]T. W. Murray, S. Krishnaswamy, and J. D. Achenbach, "Laser generation of ultrasound in films and coatings," Appl. Phys. Lett. **74**(23), 3561–3563 (1999).
[12]A. A. Maznev, A. Akthakul, and K. A. Nelson, "Surface acoustic modes in thin films on anisotropic substrates," J. Appl. Phys. **86**(5), 2818–2824 (1999).
[13]C. Bescond, S. E. Kruger, D. Lévesque, R. S. Lima, and B. R. Marple, "In-situ simultaneous measurement of thickness, elastic moduli and density of thermal sprayed WC-Co coatings by laser-ultrasonics," J. Therm. Spray Technol. **16**(2), 238–244 (2007).
[14]F. Jenot, S. Fourez, M. Ouaftouh, and M. Duquennoy, "Nondestructive testing of thin films using surface acoustic waves and laser ultrasonics," AIP Conf. Proc. **1949**, 230031 (2018).
[15]D. Schneider, T. Schwarz, A. S. Bradford, Q. Shan, and R. J. Dewhurst, "Controlling the quality of thin films by surface acoustic waves," Ultrasonics **35**(5), 345–356 (1997).
[16]D. Schneider, B. Schultrich, H.-J. Scheibe, H. Ziegele, and M. Griepentrog, "A laser-acoustic method for testing and classifying hard surface layers," Thin Solid Films **332**(1–2), 157–163 (1998).
[17]G. Watzl, S. Eder, M. Ryzy, M. Hettich, E. Scherleitner, M. Schagerl, and C. Grünsteidl, "Single-shot capable surface acoustic wave dispersion measurement of a layered plate," Rev. Sci. Instrum. **96**, 074903 (2025).
[18]D. A. Kiefer (2024) "GEWtool (computer software)," GitHub, https://github.com/dakiefer/GEWtool.

[19]F. W. Jones, "The measurement of particle size by the x-ray method," Proc. R. Soc. London, Ser. A **166**, 16–43 (1938).
[20]O. Engler and V. Randle, *Introduction to Texture Analysis: Macrotexture, Microtexture, and Orientation Mapping*, 2nd ed. (CRC Press, Boca Raton, FL, 2009).
[21]E. S. Fisher and C. J. Renken, "Single-crystal elastic moduli and the hcp → bcc transformation in Ti, Zr, and Hf," Phys. Rev. **135**(2A), A482–A494 (1964).
[22]Y. Li and R. B. Thompson, "Relations between elastic constants $C_{ij}$ and texture parameters for hexagonal materials," J. Appl. Phys. **67**(5), 2663–2665 (1990).
[23]S. Hirsekorn, "Elastic properties of polycrystals: A review," Texture, Stress, Microstruct. **12**(1-3), 1–14 (1990).
[24]R. Hill, "The elastic behaviour of a crystalline aggregate," Proc. Phys. London, Ser. A **65**, 349–354 (1952).
[25]S. I. Ranganathan and M. Ostoja-Starzewski, "Universal elastic anisotropy index," Phys. Rev. Lett. **101**(5), 055504 (2008).
[26]A. Fichtner, *Full Seismic Waveform Modelling and Inversion (Advances in Geophysical and Environmental Mechanics and Mathematics)* (Springer, Berlin, Germany, 2010).
[27]H. Gravenkamp, C. Song, and J. Prager, "A numerical approach for the computation of dispersion relations for plate structures using the Scaled Boundary Finite Element Method," J. Sound Vib. **331**(11), 2543–2557 (2012).
[28]D. A. Kiefer, *Elastodynamic Quasi-Guided Waves for Transit-Time Ultrasonic Flow Metering*, number 42 in FAU Forschungen Reihe B (FAU University Press, Erlangen, Germany, 2022).
[29]H. Gravenkamp, B. Plestenjak, and D. A. Kiefer, "Notes on osculations and mode tracing in semi-analytical waveguide modeling," Ultrasonics **135**, 107112 (2023).
[30]D. A. Kiefer, B. Plestenjak, H. Gravenkamp, and C. Prada, "Computing zero-group-velocity points in anisotropic elastic waveguides: Globally and locally convergent methods," J. Acoust. Soc. Am. **153**(2), 1386–1398 (2023).
[31]G. A. D. Briggs and O. V. Kolosov, *Acoustic Microscopy*, 2nd ed. (Oxford University Press, Oxford, UK, 2010).
[32]S. Tang, J. Yin, C. Wang, and G. Zhu, "Study on leaky Lamb waves in functionally graded composites loaded by asymmetric fluids," Waves Random Complex Medium **35**(0), 8979–8998 (2025).
[33]E. Ducasse and M. Deschamps, "Mode computation of immersed multilayer plates by solving an eigenvalue problem," Wave Motion **112**, 102962 (2022).
[34]H. Gravenkamp, B. Plestenjak, D. A. Kiefer, and E. Jarlebring, "Computation of leaky waves in layered structures coupled to unbounded media by exploiting multiparameter eigenvalue problems," J. Sound Vib. **596**, 118716 (2025).
[35]J. R. Bernstein and J. B. Spicer, "Line source representation for laser-generated ultrasound in aluminum," J. Acoust. Soc. Am. **107**(3), 1352–1357 (2000).
[36]Y. Pan, C. Rossignol, and B. Audoin, "Acoustic waves generated by a laser line pulse in a transversely isotropic cylinder," Appl. Phys. Lett. **82**(24), 4379–4381 (2003).
[37]C. B. Scruby, R. J. Dewhurst, D. A. Hutchins, and S. B. Palmer, "Quantitative studies of thermally generated elastic waves in laser-irradiated metals," J. Appl. Phys. **51**(12), 6210–6216 (1980).
[38]A. Cheng, T. W. Murray, and J. D. Achenbach, "Simulation of laser-generated ultrasonic waves in layered plates," J. Acoust. Soc. Am. **110**(2), 848–855 (2001).
[39]T. Valier-Brasier and D. Royer, *Elastic Waves in Solids 2: Radiation, Scattering, Generation* (ISTE and John Wiley & Sons, New York, 2022).
[40]B. A. Auld and G. S. Kino, "Normal mode theory for acoustic waves and its application to the interdigital transducer," IEEE Trans. Electron Devices **18**(10), 898–908 (1971).
[41]G. S. Kino, *Acoustic Waves: Devices, Imaging, and Analog Signal Processing* (Prentice Hall, Englewood Cliffs, NJ, 1987).
[42]B. A. Auld, *Acoustic Fields and Waves in Solids*, 2nd ed. (Krieger Publishing Company, Malabar, FL, 1990), Vol. 2.